AGU PUBLICATIONS

Geophysical Research Letters

RESEARCH LETTER
10.1002/2015GL065101

Key Points:
- Mercury's shape and geoid are highly correlated and show mass compensation on a global scale
- Mercury is not in hydrostatic equilibrium and has an excess of spectral power density in degree 2
- Mercury's average radius is 2439.4 km; the offset between the centers of mass and figure is 0.14 km

Supporting Information:
- Table S1

Correspondence to:
M. E. Perry,
Mark.Perry@jhuapl.edu

Citation:
Perry, M. E., et al. (2015), The low-degree shape of Mercury, *Geophys. Res. Lett.*, *42*, 6951–6958, doi:10.1002/2015GL065101.

Received 25 JUN 2015
Accepted 2 AUG 2015
Accepted article online 6 AUG 2015
Published online 12 SEP 2015

The low-degree shape of Mercury

Mark E. Perry[1], Gregory A. Neumann[2], Roger J. Phillips[3], Olivier S. Barnouin[1], Carolyn M. Ernst[1], Daniel S. Kahan[4], Sean C. Solomon[5,6], Maria T. Zuber[7], David E. Smith[7], Steven A. Hauck II[8], Stanton J. Peale[9,10], Jean-Luc Margot[11], Erwan Mazarico[2], Catherine L. Johnson[12,13], Robert W. Gaskell[13], James H. Roberts[1], Ralph L. McNutt Jr.[1], and Juergen Oberst[14,15]

[1]The Johns Hopkins University Applied Physics Laboratory, Laurel, Maryland, USA, [2]Planetary Geodynamics Laboratory, NASA Goddard Space Flight Center, Greenbelt, Maryland, USA, [3]Planetary Science Directorate, Southwest Research Institute, Boulder, Colorado, USA, [4]Jet Propulsion Laboratory, California Institute of Technology, Pasadena, California, USA, [5]Lamont-Doherty Earth Observatory, Columbia University, Palisades, New York, USA, [6]Department of Terrestrial Magnetism, Carnegie Institution of Washington, Washington, District of Columbia, USA, [7]Department of Earth, Atmospheric and Planetary Sciences, Massachusetts Institute of Technology, Cambridge, Massachusetts, USA, [8]Department of Earth, Environmental, and Planetary Sciences, Case Western Reserve University, Cleveland, Ohio, USA, [9]Department of Physics, University of California, Santa Barbara, California, USA, [10]Deceased 14 May 2015, [11]Department of Earth, Planetary, and Space Sciences, University of California, Los Angeles, California, USA, [12]Department of Earth, Ocean and Atmospheric Sciences, University of British Columbia, Vancouver, British Columbia, Canada, [13]Planetary Science Institute, Tucson, Arizona, USA, [14]German Aerospace Center, Institute of Planetary Research, Berlin, Germany, [15]MIIGAiK Extraterrestrial Laboratory, Moscow State University for Geodesy and Cartography, Moscow, Russia

Abstract The shape of Mercury, particularly when combined with its geoid, provides clues to the planet's internal structure, thermal evolution, and rotational history. Elevation measurements of the northern hemisphere acquired by the Mercury Laser Altimeter on the MErcury Surface, Space ENvironment, GEochemistry, and Ranging spacecraft, combined with 378 occultations of radio signals from the spacecraft in the planet's southern hemisphere, reveal the low-degree shape of Mercury. Mercury's mean radius is 2439.36 ± 0.02 km, and there is a 0.14 km offset between the planet's centers of mass and figure. Mercury is oblate, with a polar radius 1.65 km less than the mean equatorial radius. The difference between the semimajor and semiminor equatorial axes is 1.25 km, with the long axis oriented 15° west of Mercury's dynamically defined principal axis. Mercury's geoid is also oblate and elongated, but it deviates from a sphere by a factor of 10 less than Mercury's shape, implying compensation of elevation variations on a global scale.

1. Introduction

The long-wavelength shape or figure of a planet is a fundamental geodetic property that provides constraints on its thermal and dynamical history. The shape of a rotating planet in hydrostatic equilibrium and subject to tidal forcing can be represented by a triaxial ellipsoid, for which the flattening, *f*, is related to the planetary mass, radius, and rotation rate, and the tidal response depends, inter alia, on orbital eccentricity, natural satellites, and resonance state, if applicable. Deviations from the equilibrium shape reflect the combined effects of interior dynamics such as mantle convection, lateral variations in the radial density structure, rigidity, and mass loads. Typically, the orientation of this triaxial ellipsoid is tilted, rotated, and offset with respect to a Cartesian coordinate system aligned with the principal axes of the planet that are defined by the planet's rotational dynamics and centered at the planet's center of mass (COM). The long-wavelength geoid or gravity field provides complementary information on the first-order interior density structure of a planet. Two-way radio frequency Doppler and range measurements to the MErcury Surface, Space ENvironment, GEochemistry, and Ranging (MESSENGER) spacecraft established Mercury's long-wavelength geoid [*Smith et al.*, 2012; *Mazarico et al.*, 2014].

A corresponding description of Mercury's global shape has, until now, remained elusive. Earth-based radar observations [*Harmon et al.*, 1986; *Anderson et al.*, 1996], Mariner 10 images [*Strom et al.*, 1975], and radio frequency (RF) occultations [*Fjeldbo et al.*, 1976] of signals from Mariner 10 provided the first measurements of Mercury's radius and equatorial shape. However, the low latitudes of the radar measurements, the limited imaging coverage by Mariner 10, and its two RF occultations gave little insight into the existence or magnitude of Mercury's polar flattening. Mercury Laser Altimeter (MLA) [*Cavanaugh et al.*, 2007] observations during

MESSENGER's first and second flybys of Mercury confirmed the ellipticity of the equatorial region [*Smith et al*., 2010b], and analyses of Mercury's limb from images acquired during those flybys produced a new estimate of radius [*Oberst et al*., 2011]. MLA observations acquired from orbit about Mercury have provided topographic detail for Mercury's northern hemisphere [*Zuber et al*., 2012], but MESSENGER's eccentric orbit and high northern periapsis left most of Mercury's southern hemisphere beyond the altimeter's maximum range. Absolute elevations and long-wavelength shape from stereo photogrammetry and other image-based methods are sensitive to small errors in camera geometry. Although designed to measure Mercury's shape, limb images of the south-polar region were restricted by MESSENGER's orbit geometry [*Elgner et al*., 2014]. Thus, RF occultations obtained from MESSENGER in orbit about Mercury have provided the essential southern hemisphere data needed to understand the planet's low-degree shape.

In this paper we describe the RF occultation observations and the resulting spherical harmonic model for Mercury's shape, obtained by combining the occultation data with MLA measurements from the northern hemisphere. The shape of Mercury is represented by a triaxial ellipsoid, defined in spherical harmonics by the degree-0 term (the mean radius of planet), the three degree-1 terms (the offset of the center of figure, COF, from the COM), and the five degree-2 terms (ellipsoid axis lengths, tilt, and rotation). We discuss the results for the long-wavelength shape and its correlation with Mercury's geoid.

2. Analysis of Occultation Measurements

The RF path between the known position of MESSENGER and the observing antenna on Earth at the time corresponding to occultation defines a line, which yields the radius of Mercury at the tangent point of a smooth sphere that is centered at Mercury's COM. We used RF observations obtained with the Deep Space Network (DSN) antennas from 21 March 2011 to 21 April 2014 to measure Mercury's radius at the tangent point at the time of each observed occultation, as detailed by *Perry et al*. [2011]. The RF wavelength and the geometry of the RF source (MESSENGER), edge (surface of Mercury), and observer (DSN station) define a diffraction pattern, which, in the absence of system noise or a Mercury atmosphere, will match RF power variations observed at the DSN station. We fit the predicted diffraction pattern to the RF power history [*Perry et al*., 2011] to identify the time of occultation. Mercury's position and MESSENGER's trajectory are referenced to Mercury's COM, so the COM is also the reference for the radius measurement corresponding to each occultation time. Positions on Mercury's surface were represented in a Cartesian system X, Y, Z, as defined in 2009 by the International Astronomical Union (IAU) [*Archinal et al*., 2011]. The dynamically defined system, in which the Z axis coincides with the spin axis and the X axis points sunward or antisunward at successive perihelia, differs from the IAU 2009 definition of Mercury's coordinates by $< 0.2°$, which is one tenth of the uncertainty in the angles derived in this work.

The quality of the diffraction fit, which improves as the RF power signal-to-noise ratio (SNR) increases, contributes to uncertainty in the final occultation radius. During most occultations, MESSENGER transmitted from its low-gain antennas, and the RF power received at the DSN was low. To reduce DSN receiver noise during the start of a MESSENGER occultation by Mercury, the bandwidth of the open-loop receiver at the DSN could be narrowed to 1 kHz. Coherent (two-way) operation from MESSENGER made this possible because the downlink frequency was tied to the uplink frequency, enabling accurate predictions of the received frequency. When MESSENGER was behind Mercury as viewed from Earth, the transponder used an internal oscillator for a frequency reference. The reduced stability of this oscillator precluded knowledge of the downlink frequency to better than 1 kHz, which required a wider (4 kHz) bandwidth for the DSN receiver to capture reliably the end-of-occultation (egress) transmissions. The increased noise level associated with the wider bandwidth prevented determination of most egress times to the accuracy necessary for useful measurements of Mercury's radius. The cases with borderline SNR produce poor-quality fits, and two adjacent data points, one at the unocculted level and one in the noise, often bound the time of occultation. The few dozen occultations that occurred while MESSENGER was transmitting from a high-gain antenna have sufficient power for radius measurements during egresses. The uncertainty in the time of occultation propagates into the uncertainty in the raw radius measurement via the velocity perpendicular to the line of sight. We restricted our data set to occultations for which this uncertainty was ≤ 500 m. Refinements in the diffraction pattern fit since the work reported by *Perry et al*. [2011] have reduced these errors to 150 m on average.

Table 1. Normalized and Unnormalized Spherical Harmonic Coefficients for Degrees 0 to 2[a]

SH Coefficient	Normalized (km)	Unnormalized (km)	Comments
c_{00}	2439.36 ± 0.02	2439.36 ± 0.02	Radius. IAU value is 2439.7 km
c_{10}	−0.022 ± 0.021	−0.038 ± 0.04	COF-COM *Z*
c_{11}	0.024 ± 0.016	0.042 ± 0.03	COF-COM *X*
s_{11}	0.077 ± 0.024	0.133 ± 0.04	COF-COM *Y*
c_{20}	−0.489 ± 0.014	−1.093 ± 0.03	Polar flattening
c_{21}	−0.036 ± 0.020	−0.046 ± 0.03	*X* component of *c* axis tilt
s_{21}	0.018 ± 0.028	0.023 ± 0. 04	*Y* component of *c* axis tilt
c_{22}	0.283 ± 0.018	0.181 ± 0.01	Equatorial ellipticity
s_{22}	−0.164 ± 0.019	−0.106 ± 0.01	Rotation of *a*–*b* axes in *X*–*Y* plane

[a]All uncertainties are one-standard-deviation errors (see text). The normalization factors are given by $c_{lm} = N_{lm}\bar{c}_{lm}$; $N_{lm} = [\{(2-\delta_{0m})(2l+1)(l-m)!\}/(l+m)!]^{1/2}$, where the overbar indicates the normalized quantity and δ_{ij} is the Kronecker delta. SH denotes spherical harmonic. The complete set of coefficients for an earlier solution, truncated to degree 125, is archived in the file "gtmes_125v03_sha.tab" located at http://pds-geosciences.wustl.edu/messenger/mess-h-rss_mla-5-sdp-v1/messrs_1001/data/shadr/ [*Perry et al.*, 2013]. The earlier solution used occultation results that did not incorporate the 130 m adjustment described in section 2. This difference produced a larger COF-COM offset of 0.122 km along the *Z* axis and a larger mean radius of 2439.40 km.

Local topography displaces the occultation location both radially and horizontally from the smooth-sphere tangent point. We corrected for these displacements by first identifying the occulting feature in a stereo photoclinometry (SPC) [see *Gaskell et al.* 2008] digital terrain model (DTM). Although absolute elevations from stereo images may lack long-wavelength control, the local topography has sufficient accuracy to locate the occulting edge, which is the highest point along the RF path. As the occulting feature lies above the surrounding terrain, we adjusted the raw occultation radius measurement downward by the height of the feature relative to the average elevation in a 140 × 140 km region centered on the tangent point. The region size was chosen to be sufficiently large to include the occulting edge but was not so large as to be subject to long-wavelength errors from the DTM.

We validated the occultation results by first comparing them to MLA measurements in locations where the two data sets overlap. Raw occultation results, adjusted for curvature, should match the elevations of the pixels containing the occulting edge of a spatially smoothed MLA DTM with 64 pixels per degree. For the 75 occultations between 55°N and 85°N, the average difference between the occultation measurements and the MLA occulting edges was 4 ± 25 m, and the standard deviation in the relative difference was 150 m, in agreement with the average time-based uncertainty of the occultation radii. To then evaluate the SPC DTM that is used for topography adjustments, we performed the same comparison and found that the occultation elevations averaged 130 ± 30 m higher than the corresponding SPC pixels with a standard deviation of 330 m. Further investigation of the SPC and MLA DTMs showed that the cause of the discrepancy is a suppression in the height of crater rims and other high-relief features in the SPC DTM. We translated these results to the southern hemisphere and increased the topography adjustment by 130 m and the uncertainty to 330 m. The MLA comparison also reveals three measurements with larger errors, which may be caused by trajectory or registration errors. Along-track trajectory errors convert directly to occultation radius errors. Registration errors, which are likely in these preliminary DTMs, have the largest effect when an RF path glances the rim of a crater, and a kilometer-scale registration error can cause the projected RF path to intersect or miss the rim. Other uncertainties such as that in Mercury's COM with respect to Earth are negligible for radius measurements derived from occultations.

3. Shape Model

The shape model (Table 1) is a constrained least squares fit of spherical harmonics to the MLA and occultation data. The MLA data comprise over 25 million individual measurements of radius. For convenience, the MLA observations were averaged into 0.5° by 0.5° bins, with N_i observations in each bin. The 110,591 binned values and the 385 occultation data were fit via least squares by 16,641 spherical harmonic coefficients of degree *l* and order *m* up to 128. An uncertainty of $1/\sqrt{N_i}$ km was assigned to the binned values, and the occultations were assigned an uncertainty of 0.31 km. These values reflect the variation in height of individual observations within a bin where the altitude may vary by kilometers across an individual crater, as well as the uncertainty in the height of the DTM surrounding the occultation edge. The residuals from the least squares fit model are 0.5 km for all MLA observations and 0.3 km for occultations.

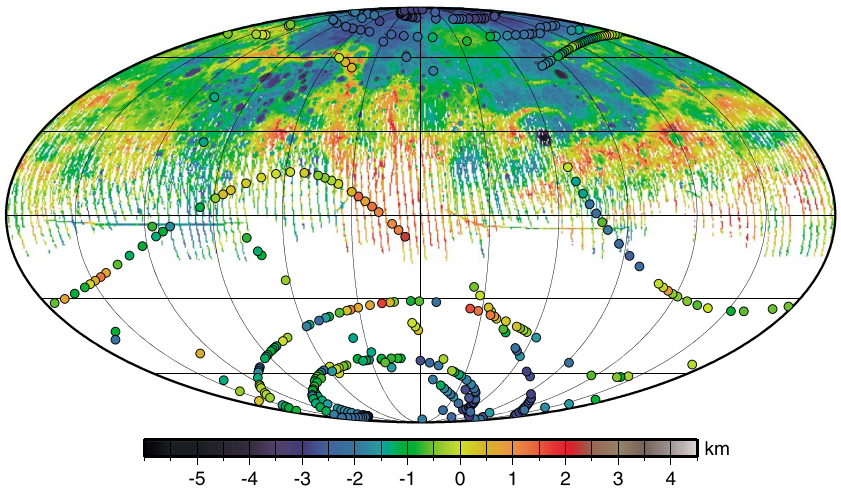

Figure 1. Locations of radius measurements from RF occultations (circles) and MLA binned data. The number and location of the occultation measurements are sufficient to determine the degree-2 shape of Mercury, but the gaps in the southern hemisphere reduce the accuracy of higher-degree-and-order terms. Both this figure and Figure 2 are Mollweide projections centered on 0° cartographic longitude. Elevations in Figures 1 and 2 are relative to a sphere of radius 2440 km. The occultation data are archived at http://pds-geosciences.wustl.edu/messenger/mess-h-rss_mla-5-sdp-v1/messrs_1001/data/occ/mess_rs_occ_v02.csv [*Perry et al.*, 2013].

The sparse distribution of data on the surface of Mercury in the southern hemisphere causes spherical harmonic solutions to be unstable. Less than 1% of the MLA observations are south of the equator, and only 227 occultation measurements lie south of 20°S (Figure 1). A weak power law constraint was applied in a manner similar to the Kaula rule [*Kaula*, 1966] commonly employed for gravity [e.g., *Mazarico et al.*, 2014] to damp the least squares equations and yield a more physically plausible solution at the expense of a negligibly worse fit to the observations. For low-degree topography of terrestrial planets, the variances by degree of $2l+1$ topography coefficients summed over order scale approximately as the inverse square of l, as noted by *Bills and Kobrick* [1985]. A damping term of $(2l+1)l^2$, the inverse of the expected variance for individual coefficients, was added to terms of degree l on the diagonal of the matrix of the normal equations, to constrain the solution variance at degrees $l>0$, leaving the (0,0) term corresponding to the mean radius unconstrained. Formal coefficient uncertainties, given as one standard deviation σ, were obtained from the diagonal terms of the solution covariance matrix and reflect the uncertainties in true coefficient power as well as the power law constraint. Thus, the formal uncertainties must be regarded as underestimates.

The physical interpretations of the spherical harmonic coefficients are given in Table 2, with the ellipsoid parameters obtained from the low-degree and low-order spherical harmonic coefficients. Neglecting the small c_{21} and s_{21} terms, the semimajor (a), intermediate (b), and semiminor (c) axes for the triaxial ellipsoid are given by [*Balmino*, 1994]

$$c_{00} = (a+b+c)/3; c_{20} = -(a+b-2c)/3; \sqrt{{c_{22}}^2 + {s_{22}}^2} = (a-b)/6. \quad (1)$$

Table 2. Parameters of a Triaxial Ellipsoid[a]

Shape Parameter	Spherical Harmonic	Triaxial Ellipsoid About COM	Comments
r (km)	2439.36 ± 0.02	2439.47	Area-averaged radius
φ	−15.2 ± 3.3°	−3.0°	Angle between long axis and X axis
θ	2.1 ± 2.4°	0° (assumed)	Angle between polar flattening axis and Z axis
a (km)	2440.53 ± 0. 04	2440.92	Semimajor (long equatorial) axis
b (km)	2439.28 ± 0.04	2439.59	Intermediate (short equatorial) axis
c (km)	2438.26 ± 0.04	2437.91	Semiminor (polar) axis

[a]The parameters are derived from the spherical harmonic coefficients (second column) and a triaxial ellipsoid fit (third column) to the MLA and occultation radii with the offset between the COF and COM set to zero.

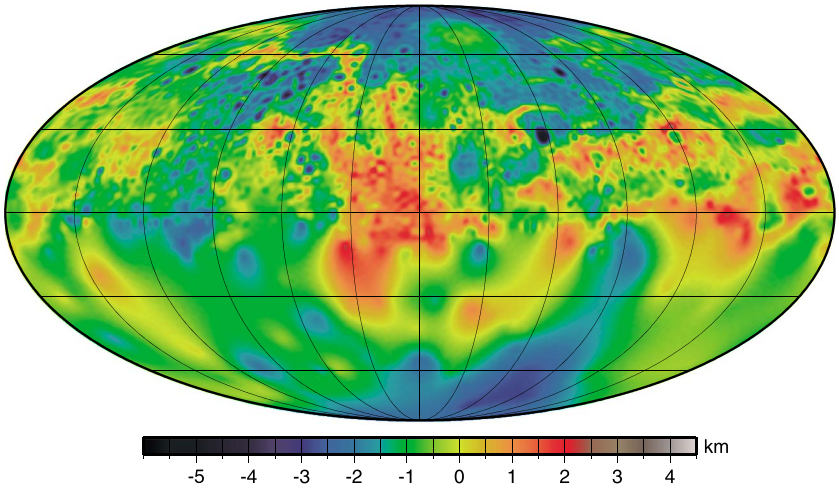

Figure 2. Shape of Mercury from a damped, spherical harmonic fit to degree and order 128 to the MLA and occultation data shown in Figure 1. Color bar gives elevation in kilometers.

The ellipsoid axes in the equatorial plane are rotated by $\phi = -15 \pm 3°$ with respect to the dynamically defined principal axes of the planet. The tilt, θ, of the ellipsoid with respect to the polar axis is between 0 and 4° (1σ). Fitting a triaxial ellipsoid directly to the MLA and occultation data produced slightly different results (Table 2), showing that the other spherical harmonic terms absorb some of the degree-2 shape.

4. Discussion

The British geophysicist *Jeffreys* [1970] was an enthusiast of planetary shape and went so far as to remark, "The determination of the Earth's axes is the main object of geodesy…" Although his remark is overstated, low-degree shape is a fundamental global property of a planet, and Jeffreys had a longstanding interest in why the second-degree shapes of the Earth and Moon departed from their hydrostatic values. The same question can now be addressed for Mercury, as the combined MLA and occultation data enable determination of the low-degree shape of Mercury. The planet's short axis is nearly aligned with its *Z* axis, and the long axis is within 15° of the dynamically defined *X* axis, the principal semimajor axis of the mass distribution. The new shape model allows determination of global flattening (discussed in detail below), as well as a specific comparison of flattening in the northern and southern hemispheres.

Flattening in the southern hemisphere is similar to that in the northern hemisphere derived from MLA data alone and reported by *Zuber et al*. [2012]. Regions within 10° of the poles are 2.23 km (southern) and 2.45 km (northern) lower in elevation than the mean equatorial elevation (Figures 2 and 3). The low elevations measured in the southern hemisphere differ sharply from initial results obtained by analyzing stereo images [*Becker et al*., 2011], which showed southern elevations similar to average equatorial elevations. The occultation results prompted additional review of the camera parameters, and slight improvements in those parameters are bringing image-based results into agreement with the occultation elevations in the southern hemisphere [*Becker et al*., 2014].

Mercury's COM-COF offset is given by $\delta X = 42 \pm 30$ m, $\delta Y = 133 \pm 40$ m, $\delta Z = -38 \pm 40$ m. The substantially larger COM-COF offsets inferred for the Moon [*Smith et al*., 2010a], Mars [*Smith et al*., 1999], and Earth [*Melosh*, 2011] have been interpreted to result from hemispheric asymmetries in crustal thickness, although the origin of those asymmetries differs among those bodies. For Earth, the offset reflects the hemisphere containing most of the continental crust versus the hemisphere centered on the Pacific Ocean basin. For Mars, the offset results from the combined effects of the thicker crust beneath the southern highlands than beneath the northern lowlands and the nearly antipodal positions of the Tharsis rise and Hellas impact basin. The lunar COM-COF offset has long been interpreted to result from the effect of thicker crust on the farside than the nearside [*Kaula*, 1975]. Among inner solar system bodies, Mercury has a small COM-COF offset relative to its radius, a situation similar to that for Venus [*Bindschadler et al*., 1994], suggesting no substantial hemispheric asymmetry in crustal thickness. Mercury's small COM-COF offset and the similar elevations at

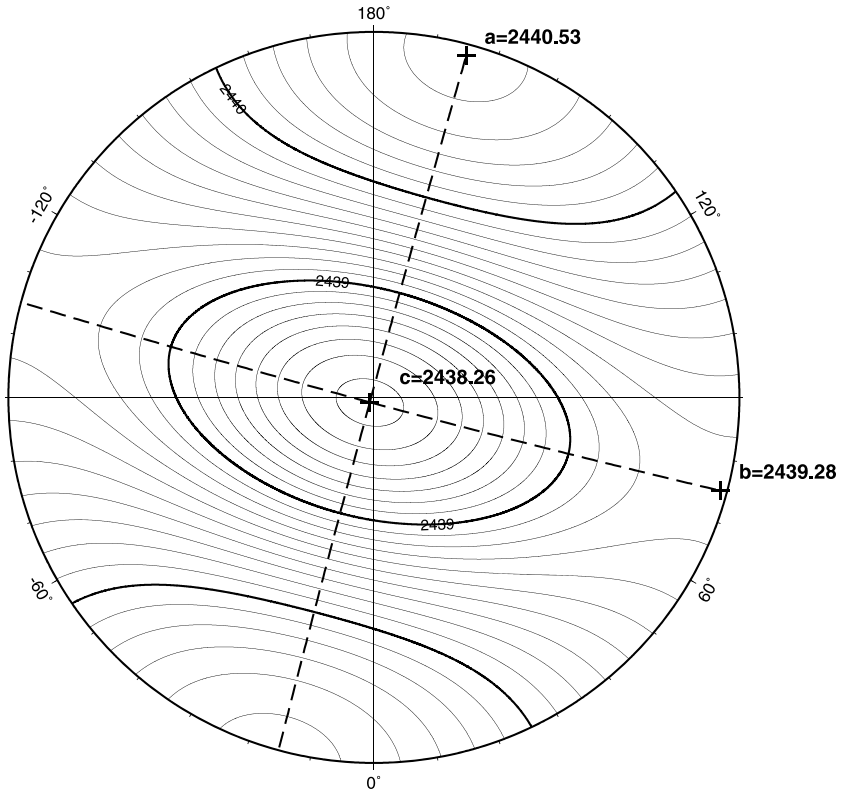

Figure 3. Shape of Mercury at spherical harmonic degree and order 2. Stereographic projection centered on the north pole and extending to the equator. The major and minor axes are each marked with a + symbol and labeled with their length. The small departure, $\theta \sim 2°$, of the semiminor axis, *c*, from the *Z* axis and the modest rotation ($\phi \sim -15°$) of the semimajor axis, *a*, from the *X* axis are seen in the displacement of the shape axes from the IAU-defined coordinate axes.

both poles are perhaps unexpected given the large expanse of northern smooth plains [*Denevi et al.*, 2013], a feature that has no counterpart in the southern hemisphere. The hemispheric asymmetry in smooth plains distribution coupled with the results here suggests that the density of the smooth plains material may differ only slightly from that of the surrounding crust.

The spherical harmonic power spectral density (PSD) of Mercury's shape is dominated by degree 2 (Figure 4) and is anomalous by extrapolation from higher degrees (an argument that has been used at the Moon to contend that the degree-2 geoid is out of hydrostatic equilibrium [*Williams et al.*, 2001]). Because degree 2 is so dominant, the full shape of Mercury is almost completely represented by a triaxial ellipsoid. Given the excess power in degree 2 and the planet's slow rotation, Mercury's shape must be well out of hydrostatic equilibrium.

Matsuyama and Nimmo [2009] provided the theory necessary to recover the hydrostatic values of the spherical harmonic coefficients, ${}^{h}c_{20}$ and ${}^{h}c_{22}$, of the shape of Mercury subject to tidal forcing, which depends on both the planet's orbital eccentricity and its 3:2 spin-orbit resonance state. One measure of the departure from the hydrostatic state is the ratio of the model shape coefficients c_{20} and c_{22} to their hydrostatic counterparts. We find values of $c_{20}/{}^{h}c_{20}$ and $c_{22}/{}^{h}c_{22}$ equal to 300 and 450, respectively, a considerable departure from the hydrostatic state. (These ratios are only lower bounds, however, because the hydrostatic numbers depend directly on h_2, the vertical displacement Love number, and we have used an upper bound, the value of h_2 for a fluid homogeneous sphere.) An additional measure, one independent of the interior rheology and density structure, is the equatorial ellipticity ratio $(b-c)/(a-c)$ [*Matsuyama and Nimmo*, 2009]. The estimated value of this quantity (0.45) is 75% of the equilibrium value of 0.59.

The substantial departure of the degree-2 shape from a hydrostatic value requires a mechanism to support the shape. Clues are provided by the corresponding degree-2 geoid. Figure 4 shows that the geoid PSD is also anomalous at degree 2 relative to extrapolation from higher degrees and, not surprisingly, is also well

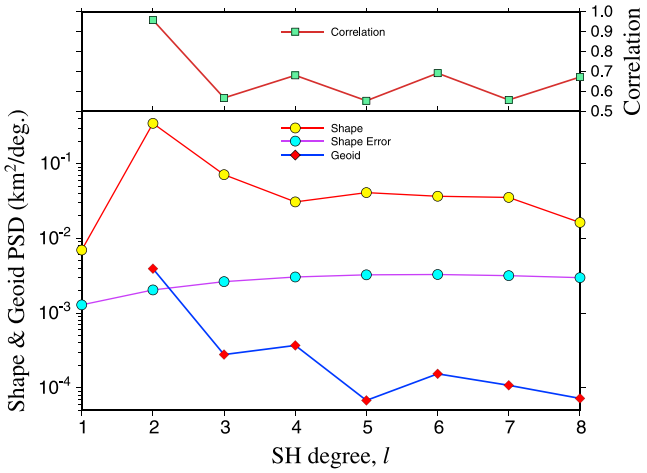

Figure 4. Power spectral density for Mercury's shape and geoid and the correlation between the two, which is particularly high at degree 2. The errors in the shape are lower bounds (see text).

out of hydrostatic equilibrium. Additional essential elements of the degree-2 shape are that the geoid has about 1% of the power of the shape but is nonetheless highly correlated (0.99) with it (Figure 4). These observations suggest that most of the degree-2 geoid signal results from the shape and that the shape must be mostly compensated, as the geoid-to-shape ratio (admittance) is 0.11 for polar flattening and equatorial ellipticity. The lack of a perfect correlation between the degree-2 shape and geoid is almost entirely due to the −15° relative rotation of the ellipsoidal axes in the equatorial plane (Figure 3). The corresponding value for the degree-2 geoid is estimated at −0.04° [*Mazarico et al.*, 2014] in a principal axis system, and theoretically is zero. The equatorial rotation of the degree-2 shape relative to the geoid is consistent with earlier findings [*Anderson et al.*, 1996; *Smith et al.*, 2010b] and may be due to asymmetries in the deep compensation but may also be an artifact of the sparse coverage at the equator.

That Mercury's degree-2 shape is a fossil relic of an earlier orbital and spin state is untenable [*Matsuyama and Nimmo*, 2009] because the semimajor axes required for Mercury's orbit are unrealistically small, only 0.05–0.06 AU given MESSENGER-derived estimates of the gravity coefficients C_{20} and C_{22} [*Mazarico et al.*, 2014]. The time required for outward migration from this position to Mercury's current orbit rivals the age of the solar system. As mentioned above, the degree-2 shape must be compensated to some degree, and the nature of the mechanisms involved lingers as a fundamental question. Compensation solely via Airy isostasy requires a pole-to-equator variation in crustal thickness of ~24 km for the crustal and mantle densities adopted by *Smith et al.* [2012]. However, scenarios for when and how global variations in crustal thickness could have formed remain to be defined and explored, and there are indications that other compensation mechanisms are involved. Mercury's mean crustal thickness is estimated to be 35 ± 18 km [*Padovan et al.*, 2015], and the degree-2 admittance (0.11) requires that a substantially deeper component of compensation exists in the mantle to support the degree-2 shape if such compensation is isostatic. Contributions from lateral variations in mantle density resulting from latitudinal and longitudinal variations in temperature associated with Mercury's insolation pattern are possible [*Phillips et al.*, 2014; *Tosi et al.*, 2014] for some fraction of the support of degree-2 shape, but at least the longitudinal variations have likely changed over Mercury's history as the planet's orbital eccentricity evolved chaotically [*Correia and Laskar*, 2009]. Other lateral variations in mantle density are also possible, including variations in the thickness of a postulated layer of solid FeS at the base of the mantle [*Smith et al.*, 2012; *Hauck et al.*, 2013; *James et al.*, 2015] and/or variations in mantle density associated with the history of mantle melt extraction. Finally, we note that an external load on an elastic lithosphere provides an alternative mechanism to satisfy the admittance constraint. This mechanism diminishes the need for a deep density source but substitutes the need to identify such a surface load. MESSENGER observations have thus established that, taken together, Mercury's low-degree shape and geoid are fundamentally different from those of the other terrestrial planets and present a challenging puzzle for the innermost planet.

Acknowledgments

MESSENGER Radio Science and altimetry data are archived in the PDS Geosciences Node http://pds-geosciences.wustl.edu. Details on MESSENGER are maintained and updated at the MESSENGER website: http://messenger.jhuapl.edu/. The MESSENGER mission is supported by the NASA Discovery Program under contracts NAS5-97271 to The Johns Hopkins University Applied Physics Laboratory and NASW-00002 to the Carnegie Institution of Washington, and the MESSENGER Participating Scientist Program. Juergen Oberst was hosted by the Moscow State University for Geodesy and Cartography (MIIGAiK) and supported by the Russian Science Foundation, under project 14-22-00197. Catherine Johnson also acknowledges support from the Natural Sciences and Engineering Research Council of Canada.

The Editor thanks Nicola Tosi and an anonymous reviewer for their assistance in evaluating this paper.

References

Anderson, J. D., R. F. Jurgens, E. L. Lau, and M. A. Slade III (1996), Shape and orientation of Mercury from radar ranging data, *Icarus*, *124*, 690–697.

Archinal, B. A., et al. (2011), Report of the IAU working group on cartographic coordinates and rotational elements: 2009, *Celest. Mech. Dyn. Astron.*, *109*, 101–135.

Balmino, G. (1994), Gravitational potential harmonics from the shape of an homogeneous body, *Celest. Mech. Dyn. Astron.*, *60*, 331–364.

Becker, K. J., L. A. Weller, K. L. Edmundson, T. L. Becker, M. S. Robinson, and S. C. Solomon (2011), Global controlled mosaic of Mercury from MESSENGER orbital images, *Eos Trans. AGU*, *92*, Fall Meet. Suppl., Abstract P41A-1589.

Becker, K. J., et al. (2014), Progress towards a global digital elevation model for Mercury, *Lunar Planet. Sci.*, *45*, Abstract 2243.

Bills, B. G., and M. Kobrick (1985), Venus topography: A harmonic analysis, *J. Geophys. Res.*, *90*, 827–836, doi:10.1029/JB090iB01p00827.
Bindschadler, D. L., G. Schubert, and P. G. Ford (1994), Venus' center of figure–center of mass offset, *Icarus*, *111*, 417–432.
Cavanaugh, J. F., et al. (2007), The Mercury Laser Altimeter instrument for the MESSENGER mission, *Space Sci. Rev.*, *131*, 451–479, doi:10.1007/s11214-007-9273-4.
Correia, A. C. M., and J. Laskar (2009), Mercury's capture into the 3/2 spin-orbit resonance including the effect of core–mantle friction, *Icarus*, *201*, 1–11.
Denevi, B. W., et al. (2013), The distribution and origin of smooth plains on Mercury, *J. Geophys. Res. Planets*, *118*, 891–907, doi:10.1002/jgre.20075.
Elgner, S., A. Stark, J. Oberst, M. E. Perry, M. T. Zuber, M. S. Robinson, and S. C. Solomon (2014), Mercury's global shape and topography from MESSENGER limb images, *Planet. Space Sci.*, *103*, 299–308, doi:10.1016/j.pss.2014.07.019.
Fjeldbo, G., A. Kliore, D. Sweetnam, P. Esposito, B. Seidel, and T. Howard (1976), The occultation of Mariner 10 by Mercury, *Icarus*, *27*, 439–444.
Gaskell, R. W., et al. (2008), Characterizing and navigating small bodies with imaging data, *Meteorit. Planet. Sci.*, *43*, 1049–1061.
Harmon, J. K., D. B. Campbell, D. L. Bindschadler, J. W. Head, and I. I. Shapiro (1986), Radar altimetry of Mercury: A preliminary analysis, *J. Geophys. Res.*, *91*, 385–401, doi:10.1029/JB091iB01p00385.
Hauck, S. A., II, S. C. Solomon, J. L. Margot, F. G. Lemoine, E. Mazarico, S. J. Peale, M. E. Perry, R. J. Phillips, D. E. Smith, and M. T. Zuber (2013), The curious case of Mercury's internal structure, *J. Geophys. Res. Planets*, *118*, 1204–1220.
James, P. B., M. T. Zuber, R. J. Phillips, and S. C. Solomon (2015), Support of long-wavelength topography on Mercury inferred from MESSENGER measurements of gravity and topography, *J. Geophys. Res. Planets*, *120*, 287–310, doi:10.1002/2014JE004713.
Jeffreys, H. (1970), *The Earth, Its Origin, History and Physical Constitution*, 5th ed., 612 pp., Cambridge Univ. Press, Cambridge, U. K.
Kaula, W. M. (1966), *Theory of Satellite Geodesy*, 124 pp., Blaisdell, Waltham, Mass.
Kaula, W. M. (1975), The gravity and shape of the Moon, *Eos Trans. AGU*, *56*, 309–316, doi:10.1029/EO056i006p00309.
Matsuyama, I., and F. Nimmo (2009), Gravity and tectonic patterns of Mercury: Effect of tidal deformation, spin-orbit resonance, nonzero eccentricity, despinning, and reorientation, *J. Geophys. Res.*, *114*, E010101, doi:10.1029/2008JE003252.
Mazarico, E., A. Genova, S. Goossens, F. G. Lemoine, G. A. Neumann, M. T. Zuber, D. E. Smith, and S. C. Solomon (2014), The gravity field, orientation, and ephemeris of Mercury from MESSENGER observations after three years in orbit, *J. Geophys. Res. Planets*, *119*, 2417–2436, doi:10.1002/2014JE004675.
Melosh, H. J. (2011), *Planetary Surface Processes*, *Cambridge Planet. Sci. Ser.*, 534 pp., Cambridge Univ. Press, Cambridge, U. K.
Oberst, J., S. Elgner, F. S. Turner, M. E. Perry, R. W. Gaskell, M. T. Zuber, M. S. Robinson, and S. C. Solomon (2011), Radius and limb topography of Mercury obtained from images acquired during the MESSENGER flybys, *Planet. Space Sci.*, *59*, 1918–1924.
Padovan, S., M. A. Wieczorek, J.-L. Margot, N. Tosi, and S. C. Solomon (2015), Thickness of the crust of Mercury from geoid-to-topography ratios, *Geophys. Res. Lett.*, *42*, 1029–1038, doi:10.1002/2014GL062487.
Perry, M. E., et al. (2011), Measurement of the radius of Mercury by radio occultation during the MESSENGER flybys, *Planet. Space Sci.*, *59*, 1925–1931.
Perry, M. E., F. G. Lemoine, D. E. Smith, M. T. Zuber, G. A. Neumann, and S. C. Solomon (2013), MESSENGER radio science reduced data record (MESS-H-RSS-5-SDP-V1. 0) NASA Planetary Data System, 2013.
Phillips, R. J., et al. (2014), Mercury's 2nd-degree shape and geoid: Lunar comparisons and thermal anomalies, *Lunar Planet. Sci.*, *45*, Abstract 2634.
Smith, D. E., et al. (1999), The global topography of Mars and implications for surface evolution, *Science*, *284*, 1495–1503, doi:10.1126/science.284.5419.1495.
Smith, D. E., et al. (2010a), Initial observations from the Lunar Orbiter Laser Altimeter (LOLA), *Geophys. Res. Lett.*, *37*, L18204, doi:10.1029/2010GL043751.
Smith, D. E., et al. (2010b), The equatorial shape and gravity field of Mercury from MESSENGER flybys 1 and 2, *Icarus*, *209*, 88–100.
Smith, D. E., et al. (2012), Gravity field and internal structure of Mercury from MESSENGER, *Science*, *336*, 214–217.
Strom, R. G., et al. (1975), Preliminary imaging results from the second Mercury encounter, *J. Geophys. Res.*, *80*, 2345–2356, doi:10.1029/JB080i017p02345.
Tosi, N., O. Cadek, S. Padovan, and M. A. Wieczorek (2014), Mercury's low-degree geoid and topography from insolation-driven elastic deformation, *Eos Trans. AGU, 95*, Fall Meeting Suppl., Abstract P21C-3937.
Williams, J. G., D. H. Boggs, C. F. Yoder, J. T. Ratcliff, and J. O. Dickey (2001), Lunar rotational dissipation in solid body and molten core, *J. Geophys. Res.*, *106*, 27,933–27,968, doi:10.1029/2000JE001396.
Zuber, M. T., et al. (2012), Topography of the northern hemisphere of Mercury from MESSENGER laser altimetry, *Science*, *386*, 217–220, doi:10.1126/science.1218805.